The Astrophysical Journal, 835:117 (10pp), 2017 February 1 doi:10.3847/1538-4357/835/2/117

Predicting the Magnetic Field of Earth-impacting CMEs

C. Kay[1], N. Gopalswamy[1], A. Reinard[2], and M. Opher[3]
[1] Solar Physics Laboratory, NASA Goddard Space Flight Center, Greenbelt, MD 20771, USA; christina.d.kay@nasa.gov
[2] University of Colorado/Cooperative Institute for Research in Environmental Sciences and National Oceanic and Atmospheric Administration/Space Weather Prediction Center, Boulder, CO 80505, USA
[3] Astronomy Department, Boston University, Boston, MA 02215, USA
Received 2016 September 15; revised 2016 December 2; accepted 2016 December 16; published 2017 January 23

Abstract

Predicting the impact of coronal mass ejections (CMEs) and the southward component of their magnetic field is one of the key goals of space weather forecasting. We present a new model, the ForeCAT In situ Data Observer (FIDO), for predicting the in situ magnetic field of CMEs. We first simulate a CME using ForeCAT, a model for CME deflection and rotation resulting from the background solar magnetic forces. Using the CME position and orientation from ForeCAT, we then determine the passage of the CME over a simulated spacecraft. We model the CME's magnetic field using a force-free flux rope and we determine the in situ magnetic profile at the synthetic spacecraft. We show that FIDO can reproduce the general behavior of four observed CMEs. FIDO results are very sensitive to the CME's position and orientation, and we show that the uncertainty in a CME's position and orientation from coronagraph images corresponds to a wide range of in situ magnitudes and even polarities. This small range of positions and orientations also includes CMEs that entirely miss the satellite. We show that two derived parameters (the normalized angular distance between the CME nose and satellite position and the angular difference between the CME tilt and the position angle of the satellite with respect to the CME nose) can be used to reliably determine whether an impact or miss occurs. We find that the same criteria separate the impacts and misses for cases representing all four observed CMEs.

Key words: Sun: coronal mass ejections (CMEs)

1. Introduction

Coronal mass ejections (CMEs) are powerful expulsions of plasma and magnetic field that routinely erupt from the Sun and propagate out through the solar system. Understanding space weather, including the changes in the electromagnetic properties of the near-Earth environment, becomes more and more important as we rely more heavily on spaceborne technology and highly interconnected electrical grids, which are sensitive to strong space weather events (e.g., Schrijver 2015). CMEs tend to drive the strongest space weather effects, so understanding the path a CME takes in the corona and in the heliosphere, if and when it will impact Earth, and what its properties will be upon impact is key for accurate space weather predictions.

Observations show that CMEs frequently do not travel on a radial path in the low corona, rather they deflect, changing their latitude and longitude (e.g., Hildner 1977; MacQueen et al. 1986; Isavnin et al. 2014). Byrne et al. (2010) measure the deflection of the 2008 December 10 CME, which deflected over 30° from a high latitude to the solar equator. This deflection caused the CME to impact Earth, which would not be expected if only the CME source location were considered. Alternatively, deflection can prevent an impact from occurring when one was initially expected (Mays et al. 2015b; Möstl et al. 2015). Understanding deflections is essential for predicting not only whether a CME will impact Earth, but which part of it may impact as well.

Magnetic forces are the most common explanation for CME deflections in the corona. CME deflections tend to follow the direction of the background solar magnetic gradients (Gui et al. 2011; Shen et al. 2011). On global scales, this corresponds to motion toward the heliospheric current sheet (HCS) and away from coronal holes (Filippov et al. 2001; Cremades & Bothmer 2004; Gopalswamy et al. 2009; Kilpua et al. 2009). During solar minimum this corresponds to primarily latitudinal deflections, but it yields a wider range of directions near solar maximum. Smaller-scale magnetic gradients, such as due to the structure of active regions in the low corona, can also influence the motion of CMEs, and may explain the rolling motion of prominences (Panasenco et al. 2011, 2013).

When a CME does impact the Earth, the magnetic field is one of the most important parameters for making space weather predictions. Observations show that the intensity of magnetic storms, as measured by the disturbance storm time (Dst) index, tends to increase with both the magnitude of the southward component of the CME's magnetic field (Yurchyshyn et al. 2005) and the product of the southward magnetic field and the CME velocity (Gopalswamy et al. 2008). The magnitude of a CME's magnetic field in interplanetary space depends on both its initial strength near the Sun and the CME expansion, which determines the rate at which the internal magnetic field decreases as it propagates. Gopalswamy et al. (2014) suggest that CMEs in solar cycle 24 may be less geoeffective due to greater CME expansion resulting from a decrease in the magnetic pressure of the external solar wind (Jian et al. 2011; Kilpua et al. 2014) relative to the internal CME pressure, further decreasing the already weakened CME magnetic field. This decrease in interplanetary CME magnetic field was also confirmed in a recent statistical study (Gopalswamy et al. 2015).

Observations suggest that CMEs can also rotate (Vourlidas et al. 2011; Thompson et al. 2012; Isavnin et al. 2014). Deflection and rotation may be used somewhat imprecisely in the literature—here we refer to deflection as a translational movement causing a change in a CME's latitude and longitude and to rotation as a change in a CME's orientation measured

about a line connecting the center of the Sun and the frontmost part of a CME (the CME nose). It is often difficult to distinguish between deflection, rotation, and expansion in the low corona (Savani et al. 2010; Nieves-Chinchilla et al. 2013). CME rotation is frequently, and unambiguously, seen in magnetohydrodynamic simulations of CMEs (e.g., Lynch et al. 2009; Kliem et al. 2012). CME rotation changes the orientation of a CME, and therefore the orientation of the CME's magnetic field, which makes space weather predictions highly sensitive to the effects of rotation. Observations and simulations show that the largest deflections and rotations occur in the corona (e.g., Isavnin et al. 2014; Kay et al. 2015b; Möstl et al. 2015) but interplanetary deflections can also occur (Wang et al. 2004, 2014; Lugaz et al. 2010; Isavnin et al. 2014), particularly when multiple CMEs interact (Xiong et al. 2007; Lugaz et al. 2012, 2013).

Most forecasting has focused on predicting the arrival times of CMEs, which means accurately understanding a CME's radial propagation. This generally involves determining a CME's position from coronagraph images, then simulating the radial motion, including any effects of drag, as the CME propagates through the background solar wind (Colaninno et al. 2013; Zhao & Dryer 2014; Hess & Zhang 2015; Mays et al. 2015a; Shi et al. 2015). These models predict the CME arrival time with 6–12 hr accuracy on average. Accurate timing also requires understanding which portion of the CME impacts the Earth and precise knowledge of the solar wind conditions. Gopalswamy et al. (2013) show that not accounting for CME deflections or the modification of the solar wind by previous CMEs can cause large errors in predictions of arrival time.

Bothmer & Schwenn (1998) provide an algorithm for determining the magnetic field of a CME that erupts from an active region based on the orientation of the active region's polarity and the global solar dipole. This algorithm provides a statistical description of the chirality and axial field orientation of CMEs, but counterexamples occur commonly. These predicted orientations can be compared with the CME's orientation when observed in situ, which requires fitting a flux rope model to the observed magnetic field (e.g., Al-Haddad et al. 2013, and references therein). The simplest flux rope model is the force-free model with constant α (Burlaga 1988), in which the magnetic tension balances the magnetic pressure gradient throughout the CME ($\nabla \times \boldsymbol{B} = \alpha \boldsymbol{B}$). Alternative methods include solving the Grad–Shafranov equation (Hu & Sonnerup 2001) or using a circular cylindrical flux rope model (Nieves-Chinchilla et al. 2016). Marubashi et al. (2015) compare the orientation of 55 CMEs, derived from in situ measurements, with the tilt angle of the polarity inversion lines of their source regions and find that the two directions typically differ by less than 30°.

Rather than using a flux rope model to determine a CME orientation from in situ data, Savani et al. (2015) reconstruct a CME from coronagraph images and use this position and orientation with the magnetic helicity and axial field orientation predicted by Bothmer & Schwenn (1998) to predict the CME's in situ magnetic field. Reconstructed CME positions and orientations have large uncertainties (Thernisien et al. 2009). In this paper we show that these uncertainties correspond to a wide range in the predicted in situ CME magnetic field. First, in Section 2 we present the ForeCAT In situ Data Observer (FIDO), a new method for creating synthetic in situ magnetic profiles driven by results from Forecasting a CME's Altered Trajectory (ForeCAT; Kay et al. 2015b). In Section 3 we compare FIDO results with four observed CMEs, and in Section 4 we explore FIDO's sensitivity to the CME's position and orientation. Finally, in Section 5 we consider the parameters that determine whether a CME impacts or misses our target satellite.

2. ForeCAT and FIDO

We first simulate a CME's coronal evolution using ForeCAT (Kay et al. 2013, 2015b), which determines the deflection and rotation using the magnetic forces from the background solar magnetic field—both magnetic tension and magnetic pressure gradients. The magnetic background, which determines these forces, is simulated using the potential field source surface (PFSS) model (Altschuler & Newkirk 1969; Schatten et al. 1969) driven by a synoptic magnetogram from the Helioseismic and Magnetic Imager on board the *Solar Dynamics Observatory*. We use the standard source surface distance of 2.5 $R_\odot$. The magnetic pressure gradients can be determined from the PFSS model, and we assume the magnetic field draping about the CME to determine the curvature required for the magnetic tension (Kay et al. 2015b).

The current version of ForeCAT (Kay et al. 2015b) models a CME flux rope as a torus (see Figure 2 of Kay et al. 2015b). The ForeCAT torus has a circular cross section, but the toroidal axis can be eliptical so that the CME width need not equal its height. The net external magnetic force on the torus causes a deflection, which we define as a change in the latitude or longitude of the CME's nose. The net torque of these forces about the CME nose causes rotation, or a change in the tilt of the CME (measured counterclockwise with respect to the solar equator). ForeCAT continually determines the forces as the CME propagates outward radially. Since the magnetic field decays rapidly in the low corona, the magnetic forces rapidly decrease. Once the forces become negligible the CME continues to deflect and rotate with constant angular momentum, which corresponds to a decreasing rate as the CME's radial distance increases (Kay & Opher 2015). Currently, ForeCAT does not allow for any deformation of the torus, and the CME's nose always points in the radial direction. Additionally, ForeCAT does not include any deflection resulting from magnetic reconnection or nonmagnetic forces. ForeCAT has been shown to successfully reproduce both the general trends in CME deflection (Kay et al. 2015b) and individual observed CME deflections and rotations (Kay et al. 2015a, 2016).

We then use the results from the ForeCAT simulation to produce synthetic in situ magnetic field profiles using FIDO. The parameters from ForeCAT, which were constrained such that the simulation matches the coronagraph observations, determine the majority of FIDO free parameters. Using the same toroidal shape as the ForeCAT model, and the location and orientation from a ForeCAT simulation, we first determine the distance between a chosen spacecraft location and the toroidal axis of the CME. If this impact parameter is less than the cross-sectional radius of the CME, then the spacecraft is within the CME and we determine the magnetic field using a circular force-free flux rope model (Burlaga 1988). The magnitudes of the toroidal and poloidal components of the

CME's magnetic field, B_t and B_p, respectively, are given by

$$B_t = B_0 J_0\left(\frac{2.4d}{b}\right) \quad (1)$$

and

$$B_p = B_0 H J_1\left(\frac{2.4d}{b}\right) \quad (2)$$

where the axial magnetic field B_0 is a constant, d is the impact parameter, b is the cross-sectional width of the CME, J_0 and J_1 are Bessel functions, and H is the handedness of the poloidal magnetic field ($=\pm 1$). The constant 2.4 causes the toroidal magnetic field to reach zero at $d = b$. The orientation of the CME upon impacting the spacecraft determines the direction of the CME's poloidal and toroidal components, which we express in geocentric solar ecliptic (GSE) coordinates to faciliate comparison with in situ data.

Observations typically show that CMEs maintain self-similar expansion in coronagraph images beyond 5 $R_\odot$ (Chen 1996; Chen et al. 1997; Wood & Howard 2009; Mierla et al. 2011). Richardson et al. (2006) show that CMEs continue expanding until 10–15 au, then maintain a constant width. This continued expansion, however, may not correspond to a constant angular width, and the angular width certainly decreases beyond 10–15 au. Richardson et al. (2006) determine that the average CME width increases by a factor of 5 between 1 and 10 au. Accordingly, we expect that our CMEs should still be expanding at 1 au, though the rate may be slower than self-similar. For simplicity, in this paper we assume that self-similar expansion continues as the CME passes the simulated spacecraft. This causes b to increase in time as the CME as a whole increases in size. As the cross-sectional area increases, the magnetic field strength should decrease to conserve magnetic flux for both the toroidal and poloidal components. The area increases in proportion to the square of the radial distance of the CME nose; we account for this by decreasing B_0 appropriately over time.

FIDO results are fully determined by 10 free parameters for the CME, many of which are determined by ForeCAT, and the latitude and longitude of the observing spacecraft. In Section 3 we advocate that using ForeCAT results for the CME latitude, longitude, and tilt is preferrable to a CME position and orientation reconstructed from coronagraph observations. Kay & Opher (2015) show that a CME deflects and rotates with constant angular momentum beyond 10 $R_\odot$. The rate of deflection and rotation decreases rapidly with distance, so that beyond 20 $R_\odot$ we expect little change in the CME latitude, longitude, and tilt. Some observations suggest that interplanetary CME deflection may occur (Wang et al. 2004, 2014; Lugaz et al. 2010; Isavnin et al. 2014), though ForeCAT results suggest that these deflections are not likely because of magnetic forces (Kay & Opher 2015).

The CME shape and size are fully described via three parameters: the angular width, the ratio of the height to the width (A in Kay et al. 2015b), and the ratio of the cross-sectional width to the width (B in Kay et al. 2015b). These three parameters have values from the ForeCAT simulations; however, we expect they may vary between the corona and 1 au. ForeCAT maintains fixed shape ratios A and B but Riley & Crooker (2004) and Nieves-Chinchilla et al. (2012) show that CMEs can "pancake" during their propagation. We allow A to decrease and B to increase from their ForeCAT values, mimicking the effects of pancaking, as well as small changes in the angular width of the CME. The force-free magnetic field model is fully determined by the magnitude of the axial magnetic field strength, B_0, and the handedness, H. In theory, both of these can be determined from the magnetic environment from which the CME erupts. We use the relations from Bothmer & Schwenn (1994) to determine the sign of B_0 and H. We check that these values match what would be predicted by examining the environment surrounding the polarity inversion line associated with each CME. Choosing an appropriate coronal magnetic field strength and extrapolating it to an appropriate corresponding value at 1 au, however, is beyond the scope of this paper, so we leave the magnitude of B_0 as an unconstrained free parameter. The results also depend on the propagation velocity of the CME, which can be found from the observations.

The final free parameter is a constant time shift. Currently, we are not attempting to simulate the CME's radial propagation and determine an arrival time. Including this time shift facilitates comparison of the synthetic in situ data with observed CMEs, and in this work we focus on reproducing the general behavior and relative magnitudes of the individual components of the magnetic field. While forecasting the arrival of southward magnetic field would in itself be useful for space weather predictions, in the future we will incorporate more features, such as predicting arrival time and B_0, which are also essential for space weather predictions.

3. Comparison with Observations

We compare the FIDO results for four CMEs with in situ observations from the magnetometer on board the *Advanced Composition Explorer* (*ACE*). As outlined in Section 2, we first perform a ForeCAT simulation, in which we constrain the free parameters so that the results match the *STEREO* observations, then use the final CME position and orientation from ForeCAT to produce FIDO results. Table 1 lists the four CMEs used in this work, which were chosen because they have clear magnetic signatures in the *ACE* data. Two of the CMEs have been simulated with ForeCAT in other works (2011 February 15 CME in Kay et al. 2017 and 2012 July 12 CME in Kay et al. 2016). Table 1 includes the date of eruption, the initial CME position used for ForeCAT (which is constrained by observations), the date the CME reaches *ACE*, and the final CME position from ForeCAT. Hereafter, we refer to all CMEs by the date of their eruption.

For each CME we compare the synthetic in situ profile from FIDO with the *ACE* observations. Figures 1–4 show the total magnetic field, $|B|$, as well as the components in GSE coordinates: B_x, B_y, and B_z. The black line corresponds to the *ACE* data and the red line corresponds to the FIDO results using the deflected and rotated CME position and orientation from ForeCAT.

3.1. 2010 April 3 CME

Figure 1 shows results for the near-Earth magnetic field of the 2010 April 3 CME. This CME erupts from the southern hemisphere and deflects 8° north and 8° east below 10 $R_\odot$, which is the final distance of all ForeCAT simulations used in this work. The deflection and rotation are negligible beyond 10 $R_\odot$, which agrees with the results of Kay & Opher (2015). The

Table 1
Initial and Final Positions of the Considered CMEs

Eruption	Lat_0 (deg)	Lon_0 (deg)	Tilt_0 (deg)	Arrival	Lat_f (deg)	Lon_f (deg)	Tilt_f (deg)
2010 Apr 3	−22.6	255.8	−44.0	2010 Apr 5	−14.4	247.6	−41.6
2011 Feb 15	−19.0	33.5	5.0	2011 Feb 18	−12.2	35.7	−12.6
2012 Jul 12	−13.0	82.0	15.0	2012 Jul 15	−13.4	85.2	15.8
2014 Sep 10	13.2	87.9	−26.0	2014 Sep 12	12.3	85.9	17.6

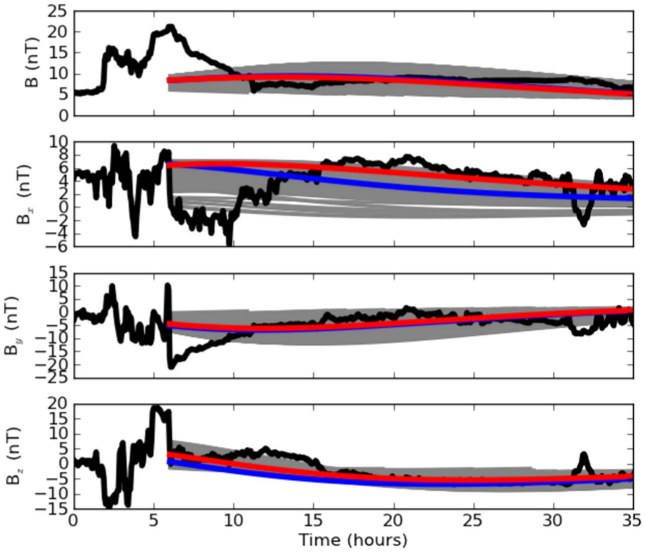

Figure 1. Comparison of the synthetic in situ profiles with *ACE* observations for the total B, B_x, B_y, and B_z (top to bottom) in GSE coordinates for the 2010 April 3 CME. The black line corresponds to the *ACE* data, the red line corresponds to FIDO results using the CME position and rotation from ForeCAT, and the blue line corresponds to assuming no deflection or rotation. The gray region shows the synthetic in situ profiles for the 150 random cases.

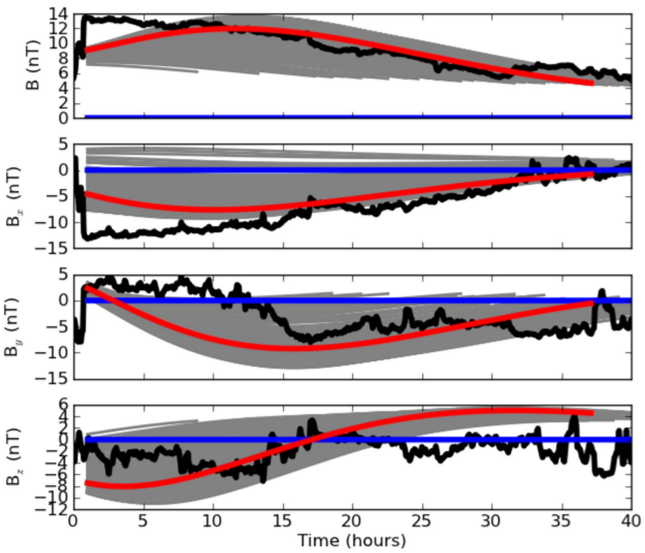

Figure 2. Same as Figure 1 but for the 2011 February 15 CME.

latitudinal motion brings the nose of the CME closer to the Earth's latitude, and the longitudinal motion moves the CME across the Earth's Carrington longitude at the time of the eruption. The CME exhibits a rotation of less than 3°. This CME drives a shock, visible before 6 hr simulation time, which we do not attempt to reproduce because it is beyond the capabilities of FIDO. Using the plasma beta we identify the

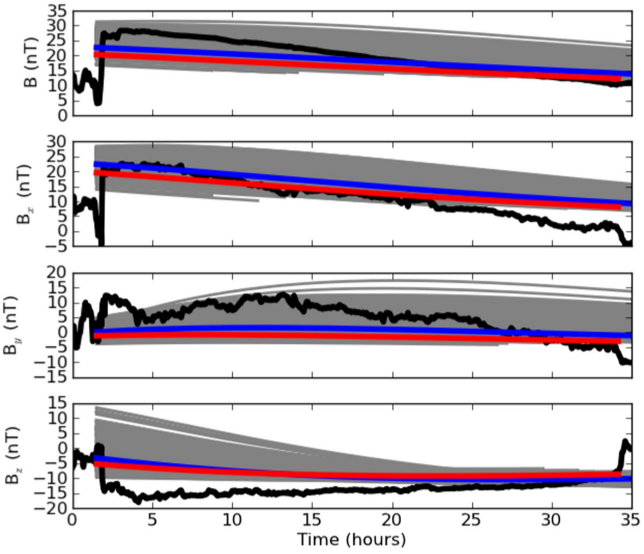

Figure 3. Same as Figure 1 but for the 2012 July 12 CME.

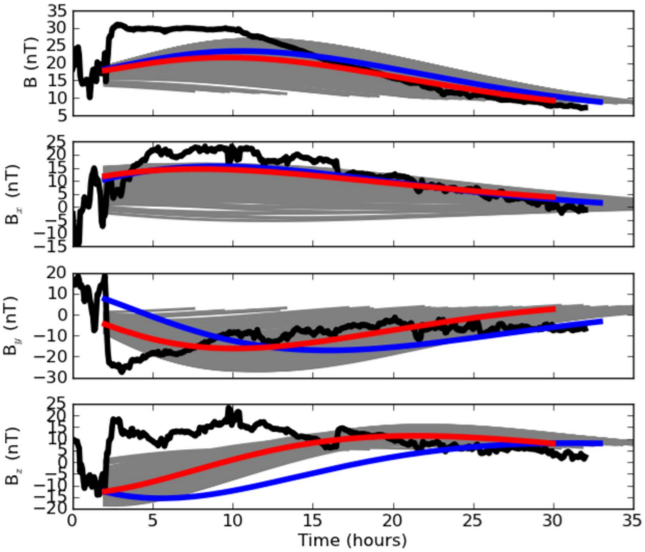

Figure 4. Same as Figure 1 but for the 2014 September 10 CME.

portion of the magnetic obstacle corresponding to the flux rope, which begins where the individual magnetic field components jump suddenly, near 6 hr simulation time. Beyond an underestimate of the magnetic field at early times, Figure 1 shows that FIDO can reproduce the majority of the general structure of the flux rope's magnetic field. We do not expect that a simple force-free model will reproduce the small-scale structure (on the scale of hours or less), which may result from dynamic effects such as reconnection or turbulence, but it can reproduce the large-scale trends and the relative magnitudes of the various components.

The magnitude of the magnetic field, B_0, is currently an unconstrained free parameter. For each of the four CMEs we scale B_0 so that the FIDO results and observations match for the largest fraction of the CME's passage. With this method, Figure 1 shows that initially we underestimate the total magnetic field of the 2010 April 3 CME, which corresponds to an underestimate in the B_x and B_y components. This enhanced magnetic field could be caused by compression near the front of the CME resulting from the expansion of the CME in the radial direction, a dynamic effect that is not included in FIDO. After the first 6 hr of CME passage (at 12 hr simulation time) we find good agreement between the synthetic and observed in situ data for all magnetic field components. The observed CME has a magnetic field that rotates from north to south, and FIDO reproduces this rotation for the duration of the CME. FIDO also captures the rotation in B_y from west to east, even when the magnitude is initially underestimated. FIDO maintains an inward radial magnetic field (positive B_x) for the duration of the CME, which matches the direction of the in situ observations beyond 10 hr simulation time, but the CME has an outward radial magnetic field for the first four hours.

We note the long extended tail seen in both the FIDO results and the in situ observations. If the simulated CME does not expand as it passes over the spacecraft, as in Savani et al. (2015), then the magnetic profiles are symmetric with respect to time. However, when we include expansion in the model, the CME is larger and has a weaker magnetic field at later times, leading to the extended tail, as is observed. The rate of expansion determines the profile of the tail. For this case, the tail is well matched by self-similar expansion.

We compare the FIDO results using the deflected and rotated CME (red line, hereafter "evolved" case) and the initial CME parameters (blue line, hereafter "radial" case), which corresponds to assuming no deflection or rotation occurs. This CME has a moderate deflection and very little rotation, so the difference between the two cases is small, but not negligible. We find that the evolved case yields a slightly better match to the observed B_x and B_z than the radial case.

3.2. 2011 February 15 CME

The 2011 February 15 CME erupted from AR 11158, a very active region that, while located near the center of the solar disk, produced 36 flares and 10 CMEs between 2011 February 12–17 (Aschwanden et al. 2014; Yashiro et al. 2014). The ForeCAT results show that the 2011 February 15 CME remains relatively constant in longitude but deflects 7° northward, bringing it closer to the Earth's latitude. While the CME exhibits only a moderate deflection, it rotates almost 18° clockwise, bringing the CME orientation more parallel to the inclination of the HCS.

Figure 2 compares the FIDO results with the *ACE* observations in the same format as Figure 1. This CME exhibits much less complex structure than the 2010 April 3 CME, having no preceding shock at 1 au and smoothly decreasing magnetic field strength. FIDO yields good matches to $|B|$ and B_x, and decent matches to B_y and B_z, though the FIDO results tend to vary more than the observations for these two components. The observed B_x slightly exceeds the FIDO results for the first 10 hr of the CME propagation but then matches well for the remainder of the CME, similar to the 2010 April 3 CME. The observed B_z remains relatively small throughout the observed CME, varying between approximately ± 5 nT. The FIDO results show a smooth variation between -8 and 4 nT, with the sign matching that of the observations in the front of the CME. Towards the back of the CME the observations fluctuate about zero whereas the simulated results transition to a small positive polarity. For B_y, the FIDO results begin with the same magnitude and sign as the observations. The simulated B_y quickly changes sign whereas the observed B_y remains relatively constant for 10 hr before changing sign. When we compare the FIDO results for the evolved and radial CMEs, we find that including the rotation and deflection is essential for this case. The radial case misses the synthetic spacecraft, so no in situ CME signature would be expected.

3.3. 2012 July 12 CME

The 2012 July 12 CME was very energetic, accompanied by an X1.4 flare and reaching a maximum speed between 1200 and 1400 km s^{-1} (Hess & Zhang 2014; Möstl et al. 2014; Shen et al. 2014). Kay et al. (2016) simulate the deflection of this CME and compare with the position of the CME reconstructed from coronagraph images to constrain its early evolution. This CME has less than 3° deflection and rotation. Because this CME propagates so rapidly, it spends very little time in the corona where the strong magnetic forces can deflect and rotate it. Kay et al. (2016) show that the initial position can be well constrained because the magnetic forces from the active region must be relatively balanced for so little deflection to occur.

Figure 3 compares the FIDO results with the observed in situ data. Note that at 1 au a second CME followed directly behind the 2012 July 12 CME. Here we compare only to the first flux rope, and assume that interaction with the trailing CME has no effect on the position and orientation of the 2012 July 12 CME. We cannot tightly constrain the cross-sectional width of the CME at 1 au from our coronal simulations, and instead use the value that best matches the in situ observations for each event. Therefore, our chosen values may reflect an influence of the trailing CME on the first CME's shape, but we allow no changes in the CME position or orientation.

Again we find that FIDO can reproduce the general behavior of the observed CME. FIDO produces the same polarity B_x and B_z as the observations, but the observed magnetic field decreases more rapidly than the synthetic in situ data. This results in a slight overestimate of B_x at late times, and an underestimate of B_z at early times. Both the synthetic and observed B_y rotate from east to west, but the synthetic B_y is much smaller than the observed B_y. In both cases, B_y is the smallest of the three vector components. We see little difference between the evolved and radial FIDO results because this CME has negligible deflection and rotation.

3.4. 2014 September 10 CME

The final CME we simulate is the 2014 September 10 CME. Similar to the 2011 February 15 CME, the 2014 September 10 CME exhibits little deflection (less than a degree in latitude, two degrees in longitude) but rotates significantly (almost 44° counterclockwise). The CME rotates due to imbalances in the active region, and the majority of the rotation occurs below 2 $R_\odot$. The CME initially rotates toward the orientation of the nearby HCS, but it quickly passes that orientation and continues rotating. As the CME propagates out radially the magnetic torques become negligible so the CME's angular momentum is conserved. The continually increasing moment

of inertia of the expanding CME causes the rotation rate to decrease, and to become negligible by 5 $R_\odot$.

The observed magnetic field of the 2014 September 10 CME, shown in Figure 4, is more complex than that of the 2011 February 15 and 2012 July 12 CMEs. Similar to the 2010 April 3 CME, we use the plasma beta to identify the flux rope portion of the in situ data. As with the 2010 April 3 CME, the FIDO results underestimate the total magnetic field strength near the front of the CME, but replicate the trailing tail well. The initial underestimate results from an underestimate of the B_y component; however, FIDO does reproduce a strong eastward B_y that decreases over the duration of the CME. FIDO reproduces the magnitude and polarity of the B_x component and matches the B_z magnitude, but initially has the opposite B_z polarity. The FIDO B_z evolves from south to north whereas the observed B_z remains northward.

Due to the large rotation, the evolved and the radial cases have significantly different synthetic in situ profiles. The B_x component is not significantly affected, which we would expect for a case such as this where the CME nose is relatively close to Earth's position. Rotation will only convert B_y and B_z when the rotation axis is parallel to the $\hat{x}$ direction. The 2011 February 15 CME has little deflection and large rotation, but we find a significant change in B_x as the CME flank hits the Earth rather than the CME nose. For the 2014 September 10 CME, both the B_y and B_z profiles of the evolved case match the observations better than the radial case. However, unlike the 2011 February 15 case, the 2014 September 10 radial case does maintain the same polarities as the evolved case.

3.5. CME Shape

We currently do not simulate any evolution between the end of the ForeCAT simulation at 10 $R_\odot$ and the CME's arrival at Earth because the deflection and rotation due to magnetic forces are typically negligible at these distances. The CME shape, however, can evolve at these distances, so the shape used in the ForeCAT simulation may not accurately represent the shape at 1 au. In ForeCAT we frequently use equal CME heights and widths ($A = 1$) and cross-sectional widths one-tenth the width ($B = 0.1$). The ForeCAT simulations for the first three CMEs used coronal shape parameters [A, B] = [1, 0.1], and the 2014 September 10 simulation used [1, 0.2], because that provided a better match between the ForeCAT results and the CME's observed coronal position. Note that we estimate the final CME position and orientation near the edge of the coronagraph field of view, but do not reconstruct the full trajectory for this work, and cannot get a precise measurement of the CME's width perpendicular to the plane of the sky. We expect the shape parameters to differ by the time the CME reaches 1 au. The cross-sectional width of the CME tends to increase from relatively thin in the low corona to a much thicker structure at greater distances (e.g., Savani et al. 2009). CMEs also tend to flatten or pancake so that their height decreases relative to their width (e.g., simulations of Riley & Crooker 2004 and Savani et al. 2011 and observations of Liu et al. 2008). We find that the in situ observations tend to be best fit by smaller values of A and larger values of B than used in the coronal simulations. The FIDO simulations in Figures 1–4 all have B between 0.3 and 0.5 (values of 0.4, 0.3, 0.5, 0.4, in chronological order), which we determine by obtaining visual matches to the in situ observations, accounting for any variation from their coronal values used in ForeCAT. The four investigated CMEs all have smaller values of A at 1 au than in the coronal simulations. The CMEs, in chronological order, have A values of 0.7, 0.8, 0.8, and 0.9. Understanding the evolution of the CME shape and the resulting shape parameters is essential for obtaining accurate in situ predictions. Future work will focus on the sensitivity to these parameters and incorporating models for their evolution.

4. Sensitivity to Position and Orientation

In Section 3 we show that FIDO can generally reproduce the in situ magnetic field of a CME using the final CME position and orientation from ForeCAT. Theoretically, good agreement could also be found using the CME position and orientation derived from coronagraph observations, as done in Savani et al. (2015). These reconstructed positions, however, have large uncertainties—approximately 5° in latitude, 10° in longitude, and 10° in tilt (Thernisien et al. 2009). This difference between the true and reconstructed CME positions and orientations can lead to significant variance in the synthetic in situ profile. We illustrate the sensitivity to the CME position and orientation in Figures 1–4 by considering 150 additional cases with latitudes within ±5° and longitudes and tilts within ±10° of the deflected and rotated ForeCAT values. If the ForeCAT values represent the "true" CME parameters, then these random cases represent the range of values one might reconstruct from coronagraph observations. The 150 random cases are shown in gray in Figures 1–4.

The random cases uniformly sample a parameter space symmetric about the ForeCAT latitude, longitude, and tilt. The synthetic in situ data from these random cases, however, are not always symmetric about ForeCAT-driven FIDO results. For the 2010 April 3 CME (Figure 1), the random cases have profiles of similar shape and fall relatively symmetrically about the ForeCAT-driven FIDO results for B_y and B_z. The majority of the random-driven cases have weaker B_x than the ForeCAT-driven results for the CME's duration. The ForeCAT-driven B_x remains negative and slowly decreases over time. Some of the random cases have positive B_x that increases during the CME passage, which does yield a better match to the first part of the CME, but does not match the majority of the observed B_x. We note that no case matches the sign of B_x for the entirety of the CME, suggesting that the mismatch with the ForeCAT-driven data is a result of the limitations of the FIDO model rather than an incorrect CME location.

Similar to B_x for the 2010 April 3 CME (Figure 1), B_x and B_y for ForeCAT-driven results are near the limits of the range filled in by the random cases for the 2011 February 15 CME (Figure 2). The majority of the random cases have B_z behavior that falls into two distinct groups. For each group B_z remains either northward or southward and the magnitude decreases during the CME's propagation. This highlights the importance of having accurate CME positions and orientations for in situ predictions. Depending on the coronagraph fit for this case a forecaster might predict a strong geomagnetic storm due a 20 nT southward magnetic field, or little to no storm due to the northward orientation. Ultimately, the observed in situ data match one of the few cases that fall in between the two extreme groups. B_z remains relatively small, and this effect is reproduced by the ForeCAT-driven FIDO results.

Figure 2 shows that the CME position and orientation have a significant effect on the in situ CME duration. For each FIDO case we show the full duration of the CME. The varying endpoints of the random gray cases can just barely be seen on the bottom of the range of B in Figure 2. The effect is more noticeable in the difference between the duration of the "evolved" and "radial" cases. The random cases have durations ranging from less than 10 hr to over 55 hr. In this work the CME shape is a free parameter and the specific values have been chosen so that the duration of the ForeCAT-driven FIDO case matches the observed duration. All of the random cases use the same CME shape as the ForeCAT-driven case. It is likely that a better match to the observed duration could be found for each random case using different shape parameters, but this is beyond the scope of this work. Future work will explore FIDO's sensitivity to the shape parameters, because using correct shape parameters is likely critical for accurate in situ predictions.

The random cases for the 2012 July 12 CME (Figure 3) are symmetric about the ForeCAT-driven case's B_x for early times during the CME's passage, but nearly all cases exceed it at later times. The observed data decrease more rapidly than any of the FIDO results, and the random results do show that the steepness of the profile can be affected by the CME's position and orientation. The random cases' range in B_y differs from all of the ranges for all of the CMEs considered in this work. Most of the ranges initially exhibit a wide spread in magnitude but the spread decreases toward the end of the CME. This results from the decrease in the magnitude of the individual components due to the CME expansion. For the 2012 July 12 CME, B_y has an apparently smaller range at the beginning of the CME than at the end. This results from the wide range in the CME duration: many of the random cases extend significantly past the end of the observed CME. For B_z we find again that the ForeCAT-driven results do not fall in the center of the random range, and they match the observed data better than the average of the random values.

For the 2014 September 10 CME (Figure 4) the random B_y and B_z are relatively symmetric about the ForeCAT-driven results. The observed B_y matches the ForeCAT-driven results and the average of the random values, but the observed B_z has the opposite sign to any of the FIDO cases for the first half of the CME. The ForeCAT-driven B_x is near the upper limit of the random range, which includes a few cases with the opposite polarity B_x to the observations.

Figures 1–4 show that a small range in latitude, longitude, and tilt, which corresponds to the observational uncertainties, corresponds to a wide range of in situ profiles. This range corresponds to not only a large uncertainty in the CME magnitude, but often also uncertainty in the polarity of individual vector components. Additionally, this wide range is frequently not centered about the profile corresponding to the average latitude, longitude, and tilt (the ForeCAT-driven results in this case). We find that the ForeCAT-driven results typically provide a better match to the observed CME than the average of the random cases, suggesting that it is essential to use an accurate CME position and orientation. Finally, we see that the CME position and orientation can have significant effects on the in situ duration of the CME. If we have accurate and precise measurements of a CME's position and orientation then we can use the CME duration to probe the CME shape.

5. CME Impacts and Misses

Figures 1–4 show the synthetic in situ data for 150 random cases. Obtaining these 150 impacting cases required simulating more than a total of 150 random cases. Despite considering a relatively small range of parameter space in CME latitude, longitude, and tilt, we find that many of the random cases do not impact the simulated spacecraft. Here we analyze which combinations of parameters yield impacts and which misses. We seek a set of parameters that could reliably be used by space weather forecasters to predict the chances of an observed CME impacting the Earth.

We compare all possible pairs of the CME latitude, longitude, and tilt, as these are the only three parameters we vary between the different random cases. Figure 5 shows the three possible pairs using these parameters. In all panels the red circles correspond to cases that impacted the satellite, and blue cases corresponds to cases that miss. The yellow star corresponds to the values from the ForeCAT simulation.

The top row of Figure 5 shows the impacts and misses for the 2010 April 3 CME. We find that CMEs that miss tend to have positions farther to the southeast, but in this region there is still some overlap with CMEs yielding impacts. We see considerable overlap between the two populations when we consider either the latitude and tilt or the longitude and tilt.

The second row of Figure 5 shows fewer misses for the 2011 February 15 CME than the previous CME. This CME has a slightly smaller latitudinal distance from the Earth than the 2010 April 3 CME, causing all but one of the random cases to be impacts. In Section 3.2 we show that the initial CME position without any deflection or rotation would also correspond to a miss, which is due primarily to the initial tilt. The simulated CME rotation exceeds the 10° uncertainty in the tilt used for the random cases.

The 2012 July 12 CME case, shown in the third row of Figure 5, also has a large number of misses. Similar to the 2011 February 15 CME, the nose of the 2012 July 12 CME has significant separation from the Earth in longitude. This CME also arrives with its nose 18° south of the Earth's latitude. The cases corresponding to impacts and misses overlap for all three combinations of the latitude, longitude, and tilt, with the overlap being the smallest when the CME latitude and tilt are compared.

The bottom row of Figure 5 shows the hits and misses for the 2014 September 10 CME. The final CME location is within 5° latitude and longitude of the Earth's position so we see relatively few misses. The best division between the groups comes from the latitude and longitude. The misses tend to have the highest latitudes and be the most eastward. These misses correspond to a wide range of tilts, sampling the entire range in the other panels.

For each CME we can find a pair of parameters that separates the impacts and misses, but the pair differs between the different CMEs. Since no pair of parameters successfully divides the impacts and misses for all four CMEs, we seek separation using a set of derived parameters that works for all CMEs. Figure 6 shows two derived parameters that tend to successfully divide the cases into impacts and misses. We illustrate the geometry of these parameters in Figure 7. Figure 7 shows a face-on view of a CME (gray shaded region). We first consider the angular distance of the satellite from the CME nose (black dot in Figure 7). When the satellite is at an angular distance less than the cross-sectional width of the CME we

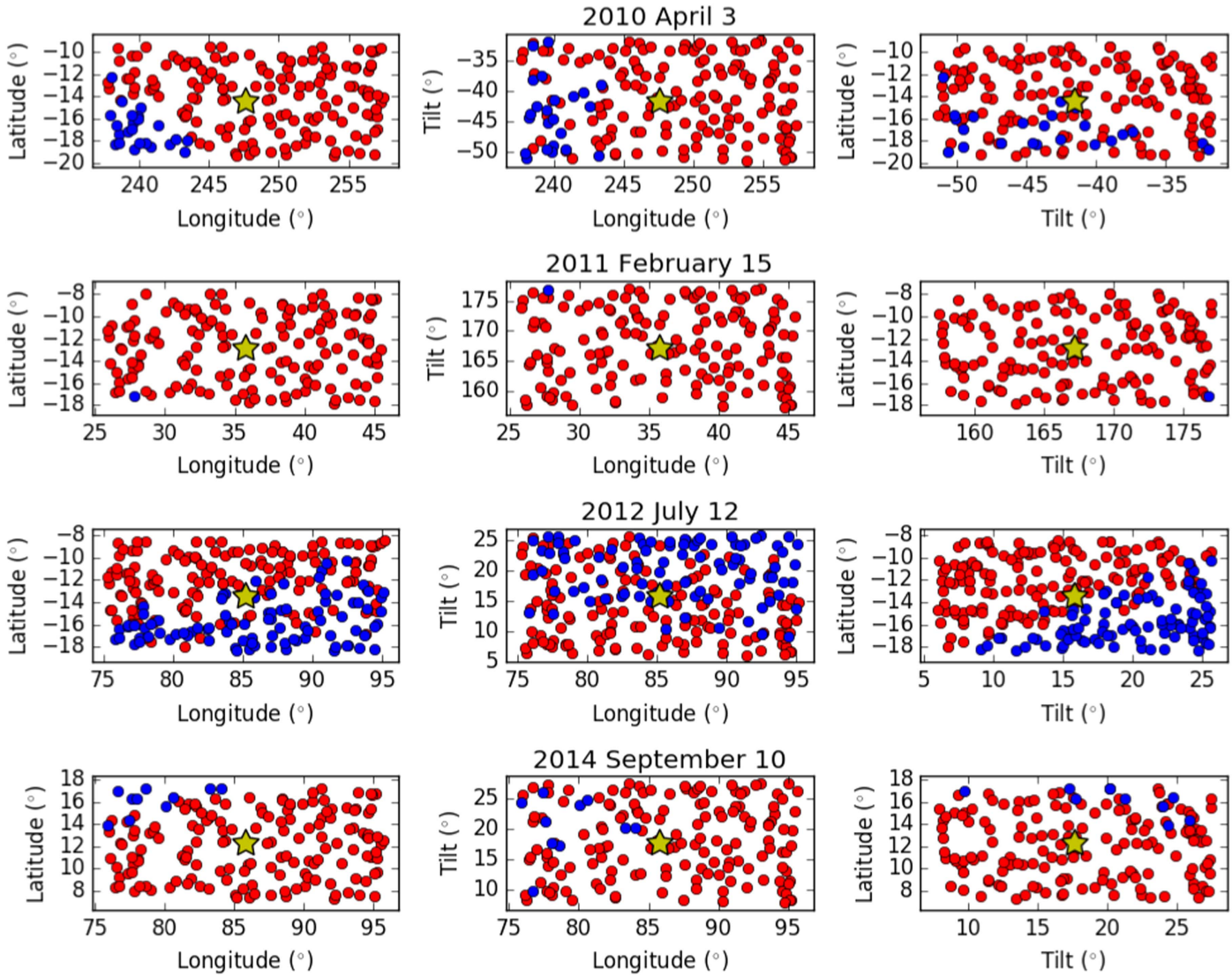

Figure 5. Comparison of parameters yielding impacts (red) and misses (blue) for the random cases. From left to right the panels show the CME latitude vs. longitude, tilt vs. longitude, and latitude vs. tilt. Each row corresponds to one of the four CMEs considered in this work.

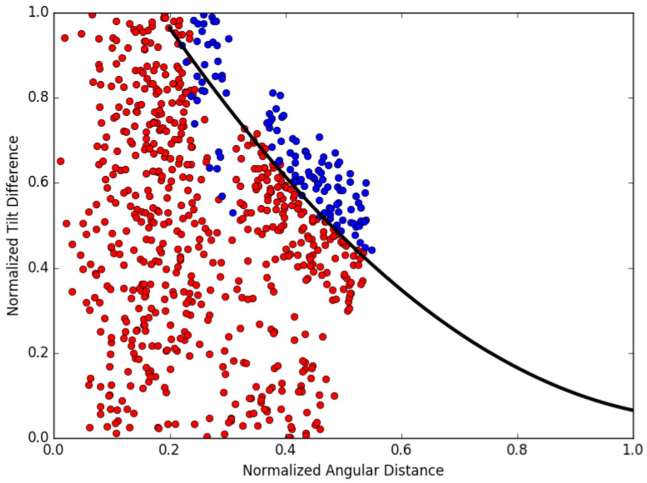

Figure 6. Comparison of the normalized angular distance and tilt difference for the four different CMEs. As in Figure 5 the red circles correspond to impacts and the blue circles to misses. The black line shows the logistic regression curve dividing the impacts and misses.

always expect that impact should occur. In Figure 7 this corresponds to region 1, the innermost dashed circle. If the angular distance is greater than the angular width of the CME then no impact should occur (large dashed circle/region 4 in Figure 7). If the angular distance is between these two widths, then impact may still occur depending on the relative location of the satellite (region 2 or 3 in Figure 7). If the satellite is close to the toroidal axis of the CME (gray dashed line in Figure 7) then impact can occur (region 2 in Figure 7). To obtain a measure of this closeness we determine the difference between the tilt of the CME and the position angle of the satellite with respect to the CME nose. Note that we consider the closest part of the CME so that this difference is never more than 90°. This allows us to divide the cases with intermediate values of angular distance. To allow for comparison between different CMEs, we normalize the angular distance by the CME width. We also normalize the tilt difference by 90° so that it spans a similar range to the normalized angular distance.

Figure 6 compares the normalized angular distance and tilt difference for all the cases for each of the four CMEs. The 2010 April 3 and 2014 September 10 CMEs both have relatively

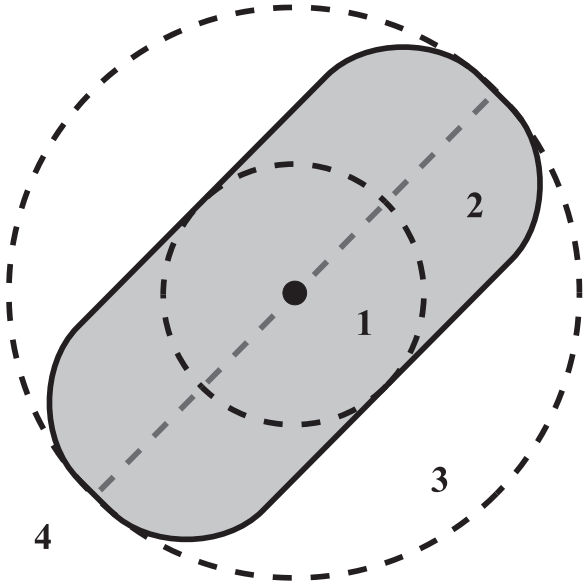

Figure 7. Cartoon illustrating the different locations with respect to the CME torus.

small normalized angular distances but exhibit a wide range in tilt difference. These two populations overlap on the left side of Figure 6. Due to the small distances, most of the CMEs correspond to impacts in region 1 of Figure 7. A small number of these distances exceed the cross-sectional width of the CME and are divided between regions 2 and 3.

The 2012 July 12 cases have larger normalized angular distances and correspond to the group in the middle of Figure 6. The CMEs mostly fall into regions 2 and 3 in Figure 7. For the 2011 February 15 cases, the angular distance is comparable to that in the 2012 July cases, but the tilt difference is much smaller and they fall in near the middle of the x-axis at the bottom of Figure 6.

Figure 6 not only shows that the normalized angular distance and tilt difference can divide the impacts and misses for each CME, but also suggests that a single line may be able divide the cases for most CMEs. The CMEs in this work have different shapes and sizes, but when normalized as such, exhibit very similar behavior. We use logistic regression to determine the dividing line between the two cases, which we show in black in Figure 6. For a given normalized angular distance, d_A, we find the tilt difference, $\Delta\gamma$, must be smaller than

$$\Delta\gamma = 1.39 - 2.37d_A + 1.04d_A^2 \quad (3)$$

for the CME to impact. This line successfully divides the majority of impacts and misses from our simulated cases, though we do see some contradicting cases. This line is not constrained for CMEs with a normalized angular distance greater than 0.5 so further cases are needed to explore its applicability in this regime. We suggest that this criterion may be useful for real-time predictions of CME impacts. In a future work we will compare these results with observed CMEs.

6. Conclusion

We have presented FIDO, which combines ForeCAT results for a CME's position and orientation with a force-free flux rope model, yielding synthetic in situ magnetic profiles. We compared FIDO results with four observed CMEs and find that FIDO typically reproduces the large-scale behavior of the observed CME's magnetic field. FIDO tends to match the polarity of each of the individual components (B_x, B_y, B_z) for each observed CME, including any changes in polarity, though we do see some disagreements. The magnitude of the CME's magnetic field is currently a free parameter, which we pick to match the observations, but the FIDO results tend to reproduce the relative magnitude of the three vector components. FIDO does not include any dynamic effects, such as from turbulence or reconnection, so we do not expect to reproduce the small-scale (hours or less) structure of the in situ data. We do find that including CME expansion is important to catch the extended tail in the magnetic profiles seen in observations.

We also show that the synthetic in situ data are highly sensitive to the CME's latitude, longitude, and tilt. We consider a range in these parameters equivalent to the uncertainty in the latitude, longitude, and tilt reconstructed from coronagraph observations. The resulting FIDO results show a wide range in CME duration and magnetic field strength, and often have the opposite polarity to the observed CME vector components. We also find that this small range in position and orientation can have an effect on whether the CME even impacts the Earth. While Marubashi et al. (2015) show that the observed CME orientations, derived from the in situ magnetic field, differ by less than 30° from the sources' polarity inversion line, this difference will have a large effect on the CME's magnetic field and the chances of CME impact. Accurately determining the magnetic profile of an Earth-impacting CME, and therefore its geoeffectiveness, requires precise knowledge of the CME's position and orientation.

FIDO results may also help us determine which CMEs are the most likely to impact Earth. For our CMEs with small variations in latitude, longitude, and tilts, we find that not every CME impacts the Earth. For each observed CME we consider we find that we can separate the synthetic CMEs into impacts or misses using some pair of these three parameters, but the same pair does not work for all CMEs. We show that we can derive a new pair of parameters—the normalized angular distance between the CME nose and satellite position and the angular difference between the CME tilt and the position angle of the satellite with respect to the CME nose—that can successfully divide the impacts and misses for all CMEs. Through logistic regression we determine the line dividing the impacts and misses, and suggest that it could be useful for predicting CME impacts and misses.

C.K.'s research was supported by an appointment to the NASA Postdoctoral Program at NASA GSFC, administered by the Universities Space Research Association under contract with NASA. The work of N.G. was supported by NASA Heliophysics Guest Investigator program. A.R. was supported by NASA grant NNH14ZDA001N-LWS.

References

Al-Haddad, N., Nieves-Chinchilla, T., Savani, N. P., et al. 2013, SoPh, 284, 129
Altschuler, M. D., & Newkirk, G. 1969, SoPh, 9, 131
Aschwanden, M. J., Sun, X., & Liu, Y. 2014, ApJ, 785, 34
Bothmer, V., & Schwenn, R. 1994, SSRv, 70, 215
Bothmer, V., & Schwenn, R. 1998, AnGeo, 16, 1
Burlaga, L. F. 1988, JGR, 93, 7217
Byrne, J. P., Maloney, S. A., McAteer, R. T. J., Refojo, J. M., & Gallagher, P. T. 2010, NatCo, 1, 74

Chen, J. 1996, JGR, 101, 27499
Chen, J., Howard, R. A., Brueckner, G. E., et al. 1997, ApJL, 490, L191
Colaninno, R. C., Vourlidas, A., & Wu, C. C. 2013, JGRA, 118, 6866
Cremades, H., & Bothmer, V. 2004, A&A, 422, 307
Filippov, B. P., Gopalswamy, N., & Lozhechkin, A. V. 2001, SoPh, 203, 119
Gopalswamy, N., Akiyama, S., Yashiro, S., et al. 2014, GeoRL, 41, 2673
Gopalswamy, N., Akiyama, S., Yashiro, S., Michalek, G., & Lepping, R. P. 2008, JASTP, 70, 245
Gopalswamy, N., Mäkelä, P., Xie, H., Akiyama, S., & Yashiro, S. 2009, JGRA, 114, A00A22
Gopalswamy, N., Mäkelä, P., Xie, H., & Yashiro, S. 2013, SpWea, 11, 661
Gopalswamy, N., Yashiro, S., Xie, H., Akiyama, S., & Mäkelä, P. 2015, JGRA, 120, 9221
Gui, B., Shen, C., Wang, Y., et al. 2011, SoPh, 271, 111
Hess, P., & Zhang, J. 2014, ApJ, 792, 49
Hess, P., & Zhang, J. 2015, ApJ, 812, 144
Hildner, E. 1977, in Study of Travelling Interplanetary Phenomena, Vol. 71 ed. M. A. Shea, D. F. Smart, & S. T. Wu (Dordrecht: D. Reidel), 3
Hu, Q., & Sonnerup, B. U. Ö. 2001, GeoRL, 28, 467
Isavnin, A., Vourlidas, A., & Kilpua, E. K. J. 2014, SoPh, 289, 2141
Jian, L. K., Russell, C. T., & Luhmann, J. G. 2011, SoPh, 274, 321
Kay, C., dos Santos, L. F. G., & Opher, M. 2015a, ApJL, 801, L21
Kay, C., Gopalswamy, N., Xie, H., & Yashiro, S. 2017, SoPh, submitted
Kay, C., & Opher, M. 2015, ApJL, 811, L36
Kay, C., Opher, M., Colaninno, R. C., & Vourlidas, A. 2016, ApJ, 827, 70
Kay, C., Opher, M., & Evans, R. M. 2013, ApJ, 775, 5
Kay, C., Opher, M., & Evans, R. M. 2015b, ApJ, 805, 168
Kilpua, E. K. J., Luhmann, J. G., Jian, L. K., Russell, C. T., & Li, Y. 2014, JASTP, 107, 12
Kilpua, E. K. J., Pomoell, J., Vourlidas, A., et al. 2009, AnGeo, 27, 4491
Kliem, B., Török, T., & Thompson, W. T. 2012, SoPh, 281, 137
Liu, Y., Luhmann, J. G., Müller-Mellin, R., et al. 2008, ApJ, 689, 563
Lugaz, N., Farrugia, C. J., Davies, J. A., et al. 2012, ApJ, 759, 68
Lugaz, N., Farrugia, C. J., Manchester, W. B., IV, & Schwadron, N. 2013, ApJ, 778, 20
Lugaz, N., Hernandez-Charpak, J. N., Roussev, I. I., et al. 2010, ApJ, 715, 493
Lynch, B. J., Antiochos, S. K., Li, Y., Luhmann, J. G., & DeVore, C. R. 2009, ApJ, 697, 1918
MacQueen, R. M., Hundhausen, A. J., & Conover, C. W. 1986, JGR, 91, 31
Marubashi, K., Akiyama, S., Yashiro, S., et al. 2015, SoPh, 290, 1371
Mays, M. L., Taktakishvili, A., Pulkkinen, A., et al. 2015a, SoPh, 290, 1775
Mays, M. L., Thompson, B. J., Jian, L. K., et al. 2015b, ApJ, 812, 145
Mierla, M., Inhester, B., Rodriguez, L., et al. 2011, JASTP, 73, 1166
Möstl, C., Amla, K., Hall, J. R., et al. 2014, ApJ, 787, 119
Möstl, C., Rollett, T., Frahm, R. A., et al. 2015, NatCo, 6, 7135
Nieves-Chinchilla, T., Colaninno, R., Vourlidas, A., et al. 2012, JGRA, 117, 6106
Nieves-Chinchilla, T., Linton, M. G., Hidalgo, M. A., et al. 2016, ApJ, 823, 27
Nieves-Chinchilla, T., Vourlidas, A., Stenborg, G., et al. 2013, ApJ, 779, 55
Panasenco, O., Martin, S., Joshi, A. D., & Srivastava, N. 2011, JASTP, 73, 1129
Panasenco, O., Martin, S. F., Velli, M., & Vourlidas, A. 2013, SoPh, 287, 391
Richardson, J. D., Liu, Y., Wang, C., & Burlaga, L. F. 2006, AdSpR, 38, 528
Riley, P., & Crooker, N. U. 2004, ApJ, 600, 1035
Savani, N. P., Owens, M. J., Rouillard, A. P., et al. 2011, ApJ, 731, 109
Savani, N. P., Owens, M. J., Rouillard, A. P., Forsyth, R. J., & Davies, J. A. 2010, ApJL, 714, L128
Savani, N. P., Rouillard, A. P., Davies, J. A., et al. 2009, AnGeo, 27, 4349
Savani, N. P., Vourlidas, A., Szabo, A., et al. 2015, SpWea, 13, 374
Schatten, K. H., Wilcox, J. M., & Ness, N. F. 1969, SoPh, 6, 442
Schrijver, C. J. 2015, SpWea, 13, 524
Shen, C., Wang, Y., Gui, B., Ye, P., & Wang, S. 2011, SoPh, 269, 389
Shen, F., Shen, C., Zhang, J., et al. 2014, JGRA, 119, 7128
Shi, T., Wang, Y., Wan, L., et al. 2015, ApJ, 806, 271
Thernisien, A., Vourlidas, A., & Howard, R. A. 2009, SoPh, 256, 111
Thompson, W. T., Kliem, B., & Török, T. 2012, SoPh, 276, 241
Vourlidas, A., Colaninno, R., Nieves-Chinchilla, T., & Stenborg, G. 2011, ApJL, 733, L23
Wang, Y., Shen, C., Wang, S., & Ye, P. 2004, SoPh, 222, 329
Wang, Y., Wang, B., Shen, C., Shen, F., & Lugaz, N. 2014, JGRA, 119, 5117
Wood, B. E., & Howard, R. A. 2009, ApJ, 702, 901
Xiong, M., Zheng, H., Wu, S. T., Wang, Y., & Wang, S. 2007, JGRA, 112, 11103
Yashiro, S., Gopalswamy, N., Mäkelä, P., et al. 2014, AdSpR, 54, 1941
Yurchyshyn, V., Yashiro, S., Abramenko, V., Wang, H., & Gopalswamy, N. 2005, ApJ, 619, 599
Zhao, X., & Dryer, M. 2014, SpWea, 12, 448